# Nodal points in three-dimensional carbon networks without inversion symmetry

Wenjie Wu, Yuee Xie,* and Yuanping Chen†
*School of Physics and Electronic Engineering, Jiangsu University, Zhenjiang, Jiangsu 212013, China*
*and School of Physics and Optoelectronics, Xiangtan University, Xiangtan, Hunan 411105, China*

(Received 4 February 2021; accepted 4 October 2021; published 20 October 2021)

Three-dimensional (3D) carbon networks provide a great platform to search and investigate various topological phases. A lot of nodal-line and nodal-surface topological phases have been found in the 3D carbon networks. However, nodal points are few in them because most carbon networks have high symmetries including inversion symmetry. Here, we propose that nodal points can be generated in low-symmetry carbon structures without inversion symmetry. Two $sp^2$-hybridized 3D carbon networks, consisting of distorted six-membered rings and a double helix, respectively, are used as examples to show nodal points. There are several pairs of nodal points locating on the high-symmetry paths of the first Brillouin zone. These nodal points are Dirac points. However, they can also be treated as Weyl points because of the negligibly small spin-orbit coupling in the carbon structures. These nodal points only shift in the momentum space but do not disappear when perturbations such as strains are applied on the carbon structures. We have also studied the topological surface states and found Fermi arcs linking the nodal points. In addition, the synthesis of two carbon networks is discussed.

DOI: 10.1103/PhysRevMaterials.5.104201

## I. INTRODUCTION

Carbon is an amazing element, not only because many carbon allotropes [from zero dimensional (0D) to three dimensional (3D)] [1–6] have been synthesized, but also because the excellent physical properties behind the allotropes shock us continuously. Recently, 3D carbon networks have attracted much attention. A lot of carbon networks [7–11] have been proposed theoretically, and some experiments have been tried to realize them [4–6,12]. These 3D carbon structures are considered good candidates for searching for new topological phases and investigating novel topological properties [11,13–23]. Many topological phases have been found in the carbon structures to date. For example, nodal lines/rings [11,13–20], (interlocking) nodal chains [21], and nodal nets [22] have been proposed and also realized in different graphene networks; nodal surfaces, nodal spheres, and nodal tubes have been generated in carbon networks consisting of nanotubes and ribbons [23].

In contrast to nodal-line and nodal-surface [24,25] topological phases, isolated nodal points were rarely found in the 3D carbon networks, although two-dimensional (2D) graphene [26] is a natural Dirac/Weyl material with Dirac/Weyl points. The most important reason is that the 3D carbon networks proposed before have high crystal symmetries including inversion, mirror, rotation axis, etc. In most cases, the crystal symmetry of a 3D nodal-point material is lower, comparing with those of 3D nodal-line and nodal-surface topological materials. It is known that carbon has negligibly small spin-orbit coupling (SOC). The carbon structures can be considered spinless systems with spin-rotational symmetry, and thus, the nodal points in the carbon structures can be regarded as Weyl points mathematically [27–30], even if they are Dirac points physically. If one wants to get a Weyl-point semimetal, the structure should have no inversion symmetry or time-reversal symmetry [30–38]. Therefore, nodal points only appear in the 3D carbon networks without inversion symmetry in the case of no external magnetic field.

The important premise of getting nodal points in 3D carbon networks is to find low-symmetry carbon structures. The 3D carbon networks proposed before are mostly made of graphene nanoribbons or carbon nanotubes. Because graphene nanoribbons and carbon nanotubes, made of hexagonal rings, have high symmetry, the 3D carbon networks made of them inherit the high symmetry. To obtain low-symmetry 3D carbon structures, one should find low-symmetry basic structural units to construct them.

In this paper, we propose two low-symmetry 3D carbon networks. The two networks are made of distorted six-membered rings and a double helix and thus named warped six-ring carbon networks (WSCNs) and double helix carbon networks (DHCNs; see Fig. 1), respectively. The symmetries of both distorted six-membered rings and double helix carbon networks are very low, and thus, WSCNs and DHCNs have low symmetry. The space group of a WSCN is $C222$, belonging to the noncentrosymmetric orthogonal crystal system, while that of a DHCN is $I422$, belonging to the noncentrosymmetric body-centered tetragonal crystal system. By checking the electronic properties of the two structures, we find that both are nodal-point semimetals with four pairs of nodal points in the momentum space. These nodal points locate on the high-symmetry paths, and they only move in the momentum space but do not disappear when perturbations such as

*yueex@ujs.edu.cn
†chenyp@ujs.edu.cn; chypxye@hotmail.com

 

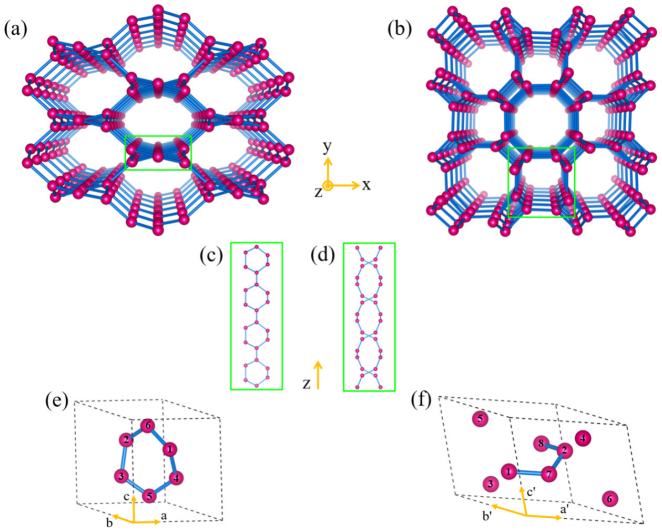


FIG. 1. Perspective views of two three-dimensional (3D) carbon networks (a) warped six-ring carbon network (WSCN) and (b) double helix carbon network (DHCN). (c) WSCN is formed by connecting warped six-membered rings, (d) while DHCN is formed by connecting double helix carbon chains. Side views of primitive cells of (e) WSCN and (f) DHCN, respectively, where the atoms are numbered.

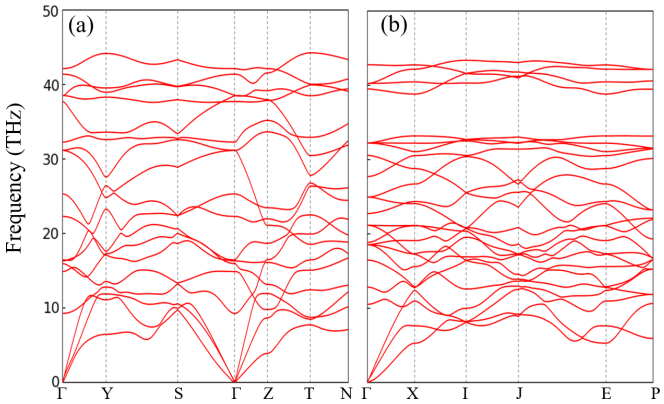


FIG. 2. Phonon dispersions of (a) warped six-ring carbon network (WSCN) and (b) double helix carbon network (DHCN).

strains are applied on the carbon structures. In addition, we analyze the topological surface states and Fermi arcs between the nodal points.

## II. MODELS AND COMPUTATIONAL METHODS

As mentioned above, 3D carbon networks with nodal points should be made of low-symmetry basic structural units. Therefore, we propose two 3D carbon networks shown in Figs. 1(a) and 1(b). The structure named a WSCN in Fig. 1(a) is formed by connecting warped six-membered rings [see Fig. 1(c)], while the structure named a DHCN in Fig. 1(b) is formed by connecting double helix carbon chains [see Fig. 1(d)]. The symmetries of both warped six-membered rings and double helix carbon chains are very low, and the two basic structural units have no inversion symmetry. Therefore, the symmetries of the two 3D carbon networks in Fig. 1 are also lower. The side views of primitive unit cells of a WSCN and a DHCN are show in Figs. 1(e) and 1(f), respectively. There are six atoms in the primitive unit cell of a WSCN and eight atoms in the primitive unit cell of a DHCN. The atomic coordinate positions in a conventional cell of a WSCN can be expressed as $8l$ (0.16951, 0.40874, 0.65781) and $4j$ (0.00000, 0.50000, 0.15808), and those in a conventional cell of a DHCN can be expressed as $16k$ (0.87965, 0.28936, 0.91029). Both are made of $sp^2$-hybridized atoms.

To calculate the electronic properties of two carbon structures, we performed first-principles calculations based on density functional theory as implemented in the Vienna *ab initio* Simulation Package (VASP) [39]. The projector augmented wave approach [40] and the generalized gradient approximation [41] described by Perdew-Burke-Ernzerhof was adopted for the potential of the core electrons and the exchange-correlation interaction between the valence electrons. The kinetic energy cutoff of 520 eV was employed. The atomic positions were optimized using the conjugate gradient method. The energy and force convergence criteria were set to be $10^{-6}$ eV and $10^{-4}$ eV/Å, respectively. The Brillouin zones (BZs) of the WSCN and the DHCN were sampled with $11 \times 11 \times 7$ and $9 \times 9 \times 9$ Monkhorst-Pack special k-point grid for optimization, respectively. The band structure and partial density of states (PDOS) were calculated by using a primitive cell. Phonon dispersions of the structures were calculated by using the force-constants method by the PHONOPY package [42]. The Fermi arc calculations were calculated by the open-source software WANNIER-TOOLS package [43].

The space group of the structure WSCN is $C222$ ($D_2^6$) (No. 21), only including three twofold rotational axes $C_{2i}$ perpendicular to the planes $k_x = 0$, $k_y = 0$, and $k_z = 0$, respectively. Its optimized lattice parameters are $a = b = 3.69$(Å) and $c = 4.49$ (Å), and the included angle $\theta$ between $a$ and $b$ is 130.68°. The bond lengths are in the range of 1.42–1.53 (Å), which are between those of diamond (1.54 Å) and graphite (1.42 Å). The space group of the structure DHCN is $I422$($D_4^9$) (No. 97), including seven rotational axes. Its optimized lattice parameters are $a' = b' = c' = 4.41$ (Å), and the bond lengths are in the range of 1.39–1.51 (Å). Because the two structures are made of distorted six-membered rings and a double helix, respectively, their crystal symmetries are lower and lack inversion symmetry. However, the two structures show good stability. The cohesive energies $E_{\rm coh}$ of the WSCN and the DHCN are −7.12 and −6.77 eV/atom, respectively. These energies are larger than those of graphite (−7.90 eV/atom) and diamond (−7.77 eV/atom) but smaller than that of T-carbon (−6.55 eV/atom). To further demonstrate dynamic stabilities of the two structures, we calculated their phonon dispersions, as shown in Figs. 2(a) and 2(b), respectively. No imaginary frequency can be found in the entire BZ. These results fully indicate that the WSCN and the DHCN are metastable carbon allotropes. In Table I, we compare structural parameters of the WSCN and the DHCN with other carbon allotropes such as T-carbon [44], bco-$C_{16}$ [17], CKL [45], IGN [11], graphite, and diamond.

TABLE I. The space group, lattice parameters, density, bond lengths, and cohesive energy of WSCN, DHCN, and some other carbon allotropes.

| Structure | Space group | Lattice parameters (Å) | | Density (g/cm$^3$) | Bond lengths (Å) | $E_{coh}$ (eV/atom) |
|---|---|---|---|---|---|---|
| | | $a = b$ | $c$ | | | |
| T-carbon | $I4_1/amd$ | 5.31 | 5.31 | 1.51 | 1.42,1.50 | −6.55 |
| DHCN | $I422(D_4^9)$ | 4.41 | 4.41 | 2.67 | 1.39–1.51 | −6.77 |
| WSCN | $C222(D_2^6)$ | 3.69 | 4.49 | 2.58 | 1.42–1.53 | −7.12 |
| bco-C16 | *IMMA* | 4.90 | 4.90 | 2.52 | 1.39–1.47 | −7.50 |
| CKL | $P6_3/mmc$ | 4.46 | 2.53 | 2.75 | 1.50,1.53 | −7.44 |
| IGN | *CMCM* | 4.33 | 2.47 | 2.59 | 1.41,1.53 | −7.62 |
| Diamond | $Fd\bar{3}m$ | 3.56 | 3.56 | 3.55 | 1.54 | −7.77 |
| Graphite | $P6_3/mmc$ | 2.46 | 6.80 | 2.24 | 1.42 | −7.90 |

## III. RESULTS AND DISCUSSIONS

In Fig. 3(a), the orbital-projection band structure of the WSCN is shown. There are four nodal points labeled as $W_1$, $W_2$, $W_3$, and $W_4$ along the high-symmetry lines $\Gamma$-$Y$, $S$-$\Gamma$, $Z$-$T$, and $T$-$N$, respectively. The right panel of Fig. 3(a) presents PDOS. The orbital projections and PDOS indicate that the crossing bands of the nodal points are attributed by orbitals $p_x$, $p_y$, and $p_z$. We further calculate wave functions of the two states $F_1$ and $F_2$ around points $W_1$ and $W_2$, respectively [see the insets in Fig. 3(a)]. One can find that the

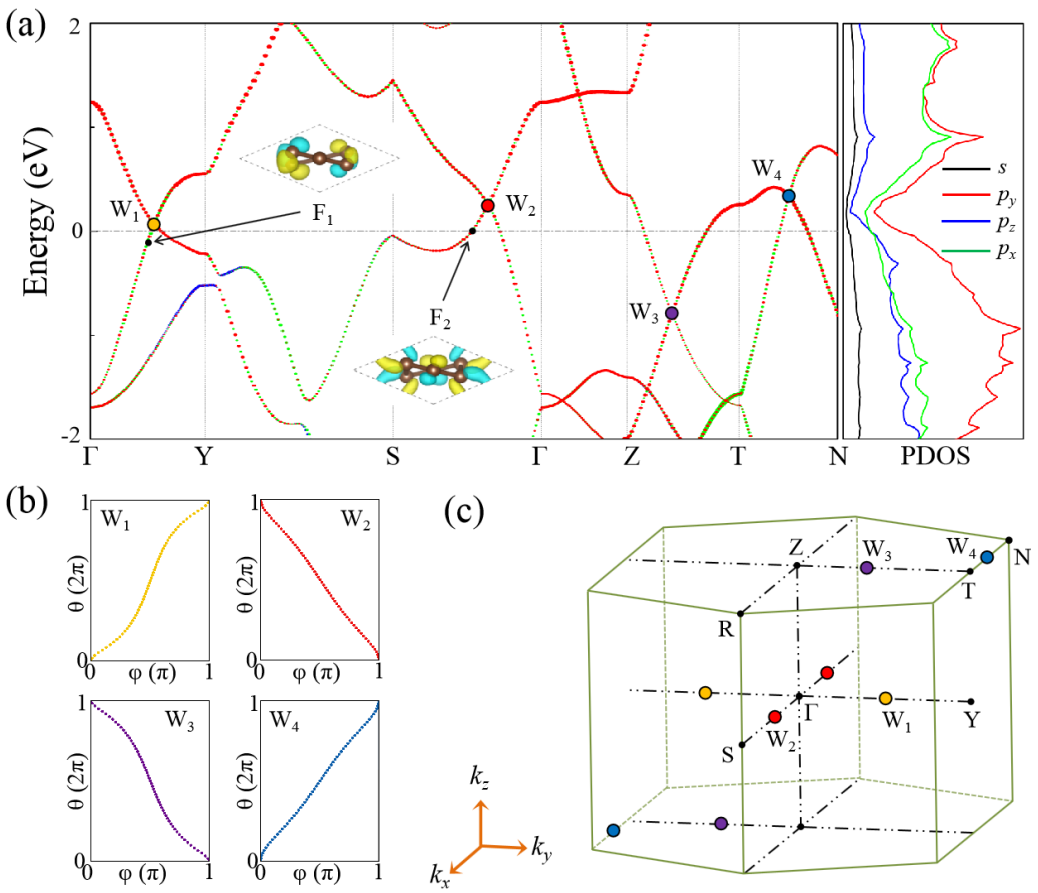


FIG. 3. (a) Orbital-projection band structure of warped six-ring carbon network (WSCN) along high-symmetry paths (left panel) and the corresponding projected density of states (PDOS; right panel), where the green, red, and blue lines (or dots) correspond to $p_x$, $p_y$, and $p_z$ orbitals of atoms, respectively. Four irreducible nodal points are labeled as $W_1$, $W_2$, $W_3$, and $W_4$. The insets show wave functions of two states $F_1$ and $F_2$ around points $W_1$ and $W_2$, respectively. (b) Evolution of the Wannier charge centers around the $W_1$, $W_2$, $W_3$, and $W_4$, respectively. The $\theta$ and $\varphi$ represent the azimuth angles of the different direction around the closed sphere enclosing the nodal point [47]. (c) Topological phase of WSCN in the first Brillouin zone (BZ), where there are four pairs of nodal points.

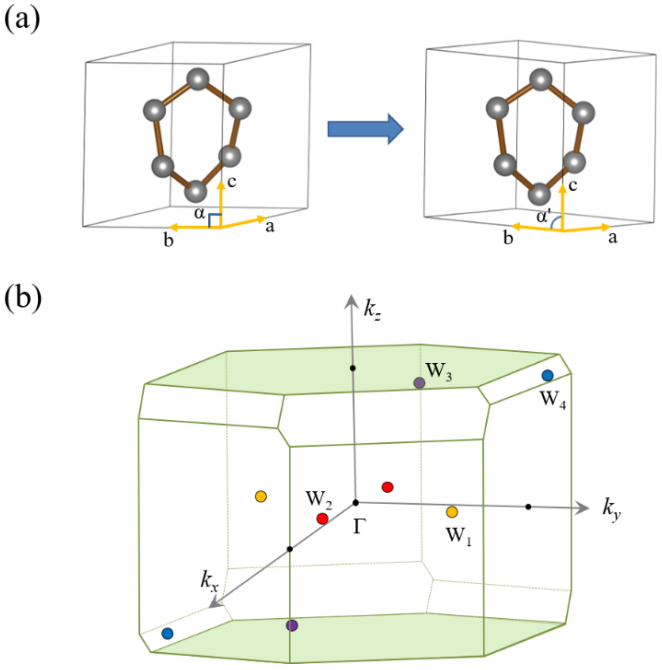


FIG. 4. (a) The included angle $\alpha$ between the lattice vectors $b$ and $c$ of warped six-ring carbon network (WSCN) varying from 90° to 85°, when a strain is applied along the line [0, 1, −1]. (b) Topological phase of WSCN in the first Brillouin zone (BZ) after strain. The four pairs of Weyl points still exist in the first BZ, but they shift away the high-symmetry lines. The coordinates of the four irreducible Weyl points are $W_1$ (0.002, 0.279, −0.008), $W_2$ (0.182, −0.027, 0.012), $W_3$ (0.005, 0.202, 0.470), and $W_4$ (−0.265, 0.495, 0.458).

orbitals are normal to the bonds, which is like the $p_z$ orbitals in graphene. Because of the negligibly small SOC in carbon materials, the carbon structures can be considered spinless systems with spin-rotational symmetry, and thus, these nodal points can be treated as Weyl points. Then the related characteristic quantities, such as Chern number and chirality, can be calculated for the nodal points.

In Weyl semimetals, the Weyl points with opposite chirality always appear in pairs. Moreover, the total number of Weyl points in a Weyl semimetal with no inversion symmetry should be a multiple of four [46]. This is because, if a structure has time-reversal symmetry, a Weyl point at momentum $k_0$ will be converted into another Weyl point at $-k_0$ with the same chirality. By checking the band crossings around the Fermi level, we find that, in the entire BZ of the WSCN, there exist four pairs of Weyl points (i.e., $W_1$, $W_2$, $W_3$, and $W_4$) locating on the planes $k_z = 0$ or $\pi$ [see Fig. 3(c)]. Each pair of Weyl points are symmetric with respect to the Γ point because of the time-reversal symmetry. To determine the chirality of the Weyl points, we calculated the Wannier charge centers of the four irreducible points [47]. As shown in Fig. 3(b), the Weyl points $W_1$ and $W_4$ have a chirality $C = +1$, while the points $W_2$ and $W_3$ have a chirality $C = -1$.

A Weyl point in a structure is robust because it cannot be removed by any small perturbations. To test the robustness, we calculate electronic properties of the WSCN in the case of all $C_2$ symmetries being destroyed. When a strain is applied along the line [0, 1, −1], the included angle $\alpha$ between the lattice vectors $b$ and $c$ of the unit cell changes from 90° to 85°, as shown in Fig. 4(a). Although this strain eliminates all $C_2$ symmetries, all the Weyl points only shift away the high-symmetry lines but still exist in the first BZ [see Fig. 4(b)]. We compare positions and energies of the four irreducible Weyl points before and after strain, as shown in Table II. The points $W_1$ and $W_2$ move away the $k_z = 0$ plane, while the points $W_3$ and $W_4$ move away the $k_z = \pi$ plane. The energies of $W_1$, $W_2$, and $W_3$ are closer to the Fermi level, but the energy of $W_4$ is farther away from the Fermi level. It means that the Weyl points are robust enough against external strains. The Weyl points can only be removed through pair annihilation, i.e., a Weyl point with chirality $C = +1$ meets another point with chirality $C = -1$. For example, the points $W_1$ and $W_2$ shift to the same point in the moment space. However, in the structure WSCN, it is very difficult to realize the shifting.

It is known that there exist Fermi arcs [48–53] between Weyl points with different chirality. We investigated surface states of the structure WSCN on the (010) surface. Two Weyl points $W_1$ are projected onto one point $\overline{W_1}$ at $\bar{\Gamma}$, and two Weyl points $W_3$ are projected onto one point $\overline{W_3}$ at $\bar{Z}$ [see Figs. 5(a) and 5(b)]. Therefore, the points $\overline{W_1}$ and $\overline{W_3}$ have chirality with $C = +2$ and $-2$, respectively. The other Weyl points $W_2$ and $W_4$ are isolated projected on the surface, and thus, their chiralities are 1 or −1. The spectral density at the Fermi level for the WSCN on the (010) surface is shown in Fig. 5(a). From point $\overline{W_1}$, there are two Fermi arcs linking two points $\overline{W_2}$, respectively. The same case occurs for $\overline{W_3}$ and $\overline{W_4}$. This coincides with the value of chirality of the points. As a comparison, we also calculate the surface states on the (001) surface, as shown in Figs. 5(c) and 5(d). Different from

TABLE II. The evolutions of locations, energies, and chirality of the four irreducible Weyl points $W_1$, $W_2$, $W_3$, and $W_4$ in the first BZ of WSCN when a strain is applied on the structure.

| Before perturbations | | | | After perturbations | | | |
|---|---|---|---|---|---|---|---|
| Nodes | $k_z(2\pi/c)$ | Energy (eV) | Chirality | Nodes | $k_z(2\pi/c)$ | Energy (eV) | Chirality |
| $W_1$ | 0.000 | 0.101 | +1 | $W_1$ | −0.008 | 0.071 | +1 |
| $W_2$ | 0.000 | 0.291 | −1 | $W_2$ | 0.012 | 0.230 | −1 |
| $W_3$ | 0.500 | −0.765 | −1 | $W_3$ | 0.470 | −0.727 | −1 |
| $W_4$ | 0.500 | 0.373 | +1 | $W_4$ | 0.458 | 0.399 | +1 |

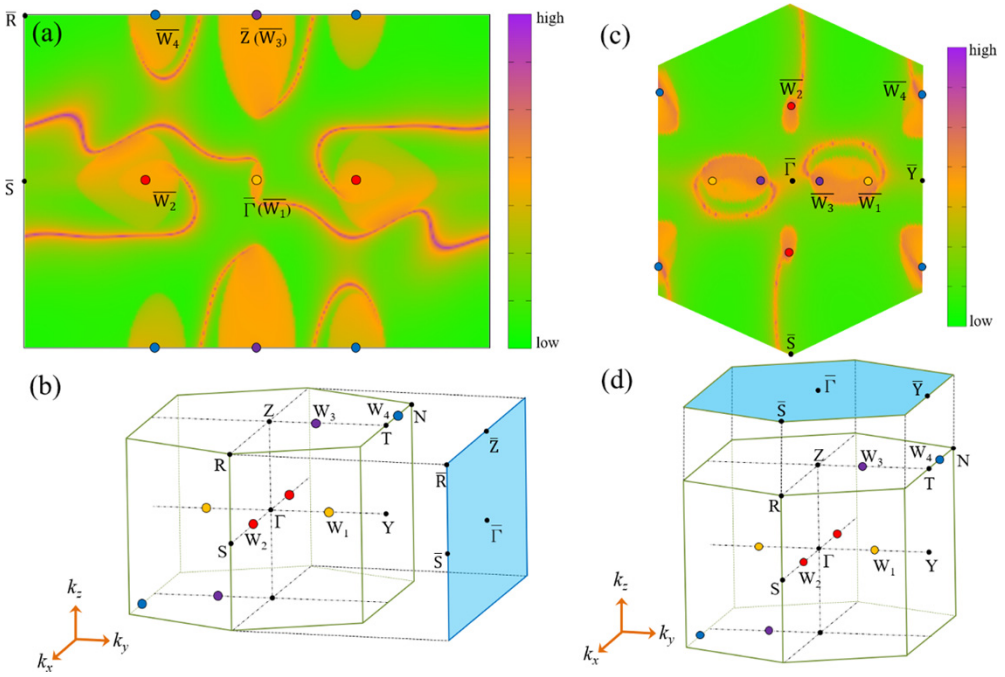


FIG. 5. (a) The spectral density at the Fermi level for the structure warped six-ring carbon network (WSCN) on the (010) surface. Four Fermi arcs crossing the boundary of the first Brillouin zone (BZ) to indirectly connect the projections of Weyl points with opposite chirality. (b) The first BZ and the corresponding (010) surface BZ. (c) The spectral density at the Fermi level for the WSCN structure on the (001) surface. Only one Fermi arc linking two Weyl points with inverse chiralities. (d) The first BZ and the corresponding (001) surface BZ.

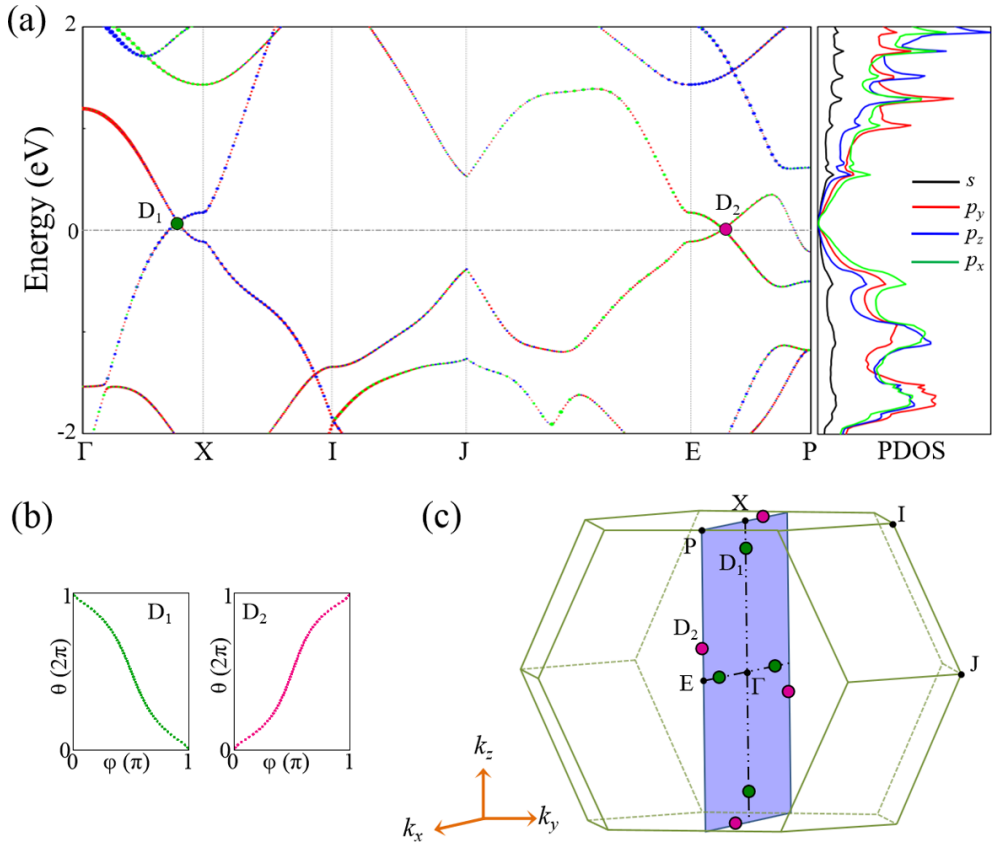


FIG. 6. (a) Orbital-projection band structure of double helix carbon network (DHCN) along high-symmetry paths (left panel) and the corresponding projected density of states (PDOS; right panel), where the green, red, and blue lines (or dots) correspond to $p_x$, $p_y$, and $p_z$ orbitals of atoms, respectively. Two Weyl points are labeled as $D_1$ and $D_2$, respectively. (b) Evolution of the Wannier charge centers around the $D_1$ and $D_2$, respectively. The $\theta$ and $\varphi$ represent the azimuth angles of the different direction around the closed sphere enclosing the Weyl point [47]. (c) Topological phase of DHCN in the first Brillouin zone (BZ), where there are four pairs of Weyl points.

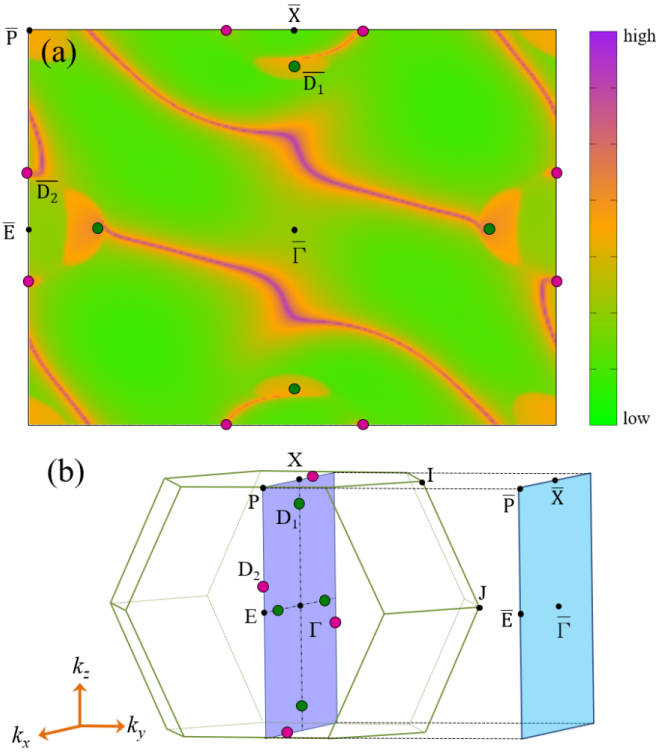


FIG. 7. (a) The spectral density at the Fermi level for the structure double helix carbon network (DHCN) on the (010) surface. Four Fermi arcs crossing the boundary of (010) surface Brillouin zone (BZ) to indirectly connect the projections of Weyl points with opposite chirality. (b) The first BZ and the corresponding (010) surface BZ.

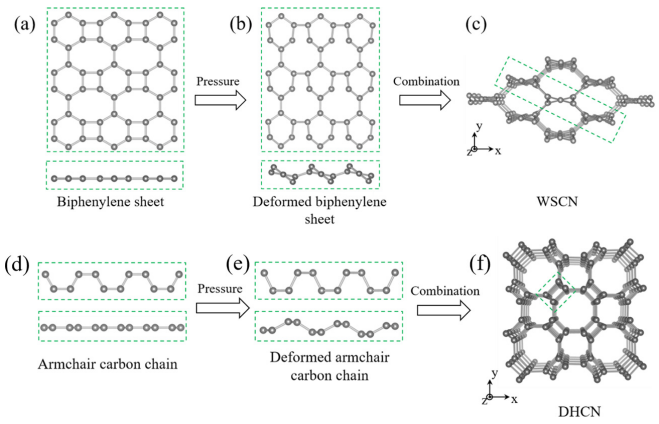


FIG. 8. Possible routines to synthesize warped six-ring carbon network (WSCN) and double helix carbon network (DHCN) structures. (a) The front view and side view of two-dimensional (2D) biphenylene sheet. (b) The front view and side view of 2D deformed biphenylene sheet. (c) The perspective view of three-dimensional (3D) WSCN structure. The green dashed box depicts the basic unit of the WSCN structure. (d) The front view and side view of one-dimensional (1D) armchair carbon chain. (e) The front view and side view of 1D deformed armchair carbon chain. (f) The perspective view of 3D DHCN structure. The green dashed box depicts the basic unit of the DHCN structure.

the case of the (010) surface, all the Weyl points are only projected onto one point on the (001) surface, respectively. Therefore, one can find that there is only one Fermi arc linking two Weyl points with inverse chiralities $\overline{W_1}$ and $\overline{W_3}$ (or $\overline{W_2}$ and $\overline{W_4}$).

Figure 6(a) presents the orbital-projection band structure of the DHCN. There are two Weyl points labeled as $D_1$ and $D_2$ along the high-symmetry lines $\Gamma$-$X$ and $E$-$P$, respectively. Due to the special symmetry of the DHCN, the band structure in the high-symmetry line $G$-$X$-$P$ is the same to that of $G$-$E$-$P$ [see Fig. S1 in the Supplemental Material] [54]. The corresponding PDOS of the band structure can be seen in the right panels of Fig. 6(a). Like the case of the structure WSCN, the crossing bands of points $D_1$ and $D_2$ are attributed by orbitals $p_x$, $p_y$, and $p_z$ because the carbon atoms in the helix are somewhat like those in the distorted hexagonal rings. By checking the band crossings around the Fermi level, we find that there also exist four pairs of Weyl points in the first BZ of the DHCN. Different from the WSCN, the four pairs of Weyl points in the DHCN all locate on the plane $k_y = 0$, as shown in Fig. 6(c). Because of the crystal symmetry and time-reversal symmetry, the four pairs of Weyl points only have two types of irreducible points, i.e., $D_1$ and $D_2$. In Fig. 5(b), the calculated Wannier charge centers of the two irreducible points indicate that the point $D_1$ has a chirality $C = -1$, while the point $D_2$ has a chirality $C = +1$. We also calculate the surface states for the structure DHCN on the (010) surface, as shown in Fig. 7. There exist four Fermi arcs linking two Weyl points with opposite chirality [see Fig. 7(a)].

In addition to the crossing points near the Fermi level, one can note that there are some other crossing points far away from the Fermi level in Figs. 3(a) and 6(a). After calculating their topological number, we find that some crossing points are also Weyl points, but some others are not (the detail is given in Fig. S2 in the Supplemental Material [54]).

In addition, inspired by the successful synthesis of atomically thin hexagonal diamond with compression [55], we propose a process to synthesize the WSCN and the DHCN. As shown in Fig. 8, the 2D biphenylene sheet has been synthesized experimentally [56], so one can compress the biphenylene sheet to get the basic unit of the WSCN structure [i.e., the deformed biphenylene sheet in Fig. 8(b)]. Then the deformed biphenylene sheets are compressed and combined in a specific manner to get a 3D WSCN structure. Similarly, as shown in Figs. 8(d) and 8(f), one can compress the one-dimensional (1D) armchair carbon chain into the basic unit of the DHCN structure [i.e., the deformed armchair carbon chain in Fig. 8(e)]. Then the deformed armchair carbon chains are compressed and combined in a specific manner to get a 3D DHCN structure.

## IV. CONCLUSIONS

In summary, to find nodal-point semimetals in 3D carbon networks, we propose two types of low-symmetry carbon networks without inversion symmetry. The two carbon networks,

named the WSCN and the DHCN, are formed by warped six-membered rings and double helix carbon chains, respectively. Their cohesive energies and phonon dispersions indicate that the two structures are metastable carbon allotropes. By using first-principles calculations, we find that the two carbon networks possess four pairs of nodal points with opposite chirality in the first BZ. These nodal points can be treated as Weyl points mathematically, even if they are Dirac points physically. When some perturbations are applied on the structures, these nodal points only move in the momentum space but do not disappear. On the structural surfaces, there are four Fermi arcs linking two nodal points with opposite chirality.

In this paper, we not only propose two $sp^2$-hybridized 3D carbon allotropes without inversion symmetry, which could be synthesized by compressing the 2D biphenylene sheets and the 1D armchair carbon chain, but also provide a method to find nodal-point semimetals in carbon networks.

## ACKNOWLEDGMENTS

This paper was supported by the National Natural Science Foundation of China (No. 12174157, No. 12074150, and No. 11874314) and the Natural Science Foundation of Hunan Province, China (No. 2018JJ2377).

[1] R.-S. Zhang and J.-W. Jiang, The art of designing carbon allotropes, Front. Phys. **14**, 13401 (2018).

[2] A. Hirsch, The era of carbon allotropes, Nat. Mater. **9**, 868 (2010).

[3] N. J. Coville, S. D. Mhlanga, E. N. Nxumalo, and A. Shaikjee, A review of shaped carbon nanomaterials, S. Afr. J. Sci. **107**, 44 (2011).

[4] Z. Chen, W. Ren, L. Gao, B. Liu, S. Pei, and H. M. Cheng, Three-dimensional flexible and conductive interconnected graphene networks grown by chemical vapour deposition, Nat. Mater. **10**, 424 (2011).

[5] Y. Ito, Y. Tanabe, H. J. Qiu, K. Sugawara, S. Heguri, N. H. Tu, K. K. Huynh, T. Takahashi, K. Tanigaki, and M. Chen, High-quality three-dimensional nanoporous graphene, Angew. Chem., Int. Ed. **53**, 4822 (2014).

[6] N. V. Krainyukova and E. N. Zubarev, Carbon Honeycomb High Capacity Storage for Gaseous and Liquid Species, Phys. Rev. Lett. **116**, 055501 (2016).

[7] Z. W. Li, Y. E. Xie, and Y. P. Chen, Three-dimensional Kagome graphene networks and their topological properties, Comput. Mater. Sci. **173**, 109406 (2020).

[8] Y. Chen, Y. Xie, Y. Gao, P.-Y. Chang, S. Zhang, and D. Vanderbilt, Nexus networks in carbon honeycombs, Phys. Rev. Mater. **2**, 044205 (2018).

[9] C. Zhong, Y. Xie, Y. Chen, and S. Zhang, Coexistence of flat bands and Dirac bands in a carbon-Kagome-lattice family, Carbon **99**, 65 (2016).

[10] C. Zhong, Y. Chen, Z. M. Yu, Y. Xie, H. Wang, S. A. Yang, and S. Zhang, Three-dimensional pentagon carbon with a genesis of emergent fermions, Nat. Commun. **8**, 15641 (2017).

[11] Y. Chen, Y. Xie, S. A. Yang, H. Pan, F. Zhang, M. L. Cohen, and S. Zhang, Nanostructured carbon allotropes with Weyl-like loops and points, Nano. Lett. **15**, 6974 (2015).

[12] M. Hu, J. He, Z. Zhao, T. A. Strobel, W. Hu, D. Yu, H. Sun, L. Liu, Z. Li, M. Ma, Y. Kono, J. Shu, H. Mao, Y. Fei, G. Shen, Y. Wang, S. J. Juhl, J. Y. Huang, Z. Liu, B. Xu, and Y. Tian, Compressed glassy carbon: An ultrastrong and elastic interpenetrating graphene network, Sci. Adv. **3**, e1603213 (2017).

[13] Z.-Z. Li, J. Chen, S. Nie, L. Xu, H. Mizuseki, H. Weng, and J.-T. Wang, Orthorhombic carbon oC24: A novel topological nodal line semimetal, Carbon **133**, 39 (2018).

[14] Y. Cheng, J. Du, R. Melnik, Y. Kawazoe, and B. Wen, Novel three dimensional topological nodal line semimetallic carbon, Carbon **98**, 468 (2016).

[15] H.-J. Sung, S. Kim, I.-H. Lee, and K. J. Chang, Semimetallic carbon allotrope with a topological nodal line in mixed $sp^2 - sp^3$ bonding networks, NPG Asia Mater. **9**, e361 (2017).

[16] H. Weng, Y. Liang, Q. Xu, R. Yu, Z. Fang, X. Dai, and Y. Kawazoe, Topological node-line semimetal in three-dimensional graphene networks, Phys. Rev. B **92**, 045108 (2015).

[17] J. T. Wang, H. Weng, S. Nie, Z. Fang, Y. Kawazoe, and C. Chen, Body-Centered Orthorhombic $C_16$: A Novel Topological Node-Line Semimetal, Phys. Rev. Lett. **116**, 195501 (2016).

[18] Y. Cheng, X. Feng, X. Cao, B. Wen, Q. Wang, Y. Kawazoe, and P. Jena, Body-centered tetragonal C16: a novel topological node-line semimetallic carbon composed of tetrarings, Small **13**, 1602894 (2017).

[19] Y. Gao, Y. Chen, Y. Xie, P.-Y. Chang, M. L. Cohen, and S. Zhang, A class of topological nodal rings and its realization in carbon networks, Phys. Rev. B **97**, 121108(R) (2018).

[20] S. Wang, Z. Peng, D. Fang, and S. Chen, A new Dirac nodal-ring semimetal made of 3D cross-linked graphene networks as lithium ion battery anode materials, Nanoscale **12**, 12985 (2020).

[21] Z. Li, Y. Xie, P.-Y. Chang, and Y. Chen, Interlocking nodal chains and their examples in carbon networks, Carbon **157**, 563 (2020).

[22] J. T. Wang, S. Nie, H. Weng, Y. Kawazoe, and C. Chen, Topological Nodal-Net Semimetal in a Graphene Network Structure, Phys. Rev. Lett. **120**, 026402 (2018).

[23] S. Z. Chen, S. Li, Y. Chen, and W. Duan, Nodal flexible-surface semimetals: case of carbon nanotube networks, Nano. Lett. **20**, 5400 (2020).

[24] C. Zhong, Y. Chen, Y. Xie, S. A. Yang, M. L. Cohen, and S. B. Zhang, Towards three-dimensional Weyl-surface semimetals in graphene networks, Nanoscale **8**, 7232 (2016).

[25] W. Wu, Y. Liu, S. Li, C. Zhong, Z.-M. Yu, X.-L. Sheng, Y. X. Zhao, and S.-A. Yang, Nodal surface semimetals: Theory and material realization, Phys. Rev. B **97**, 115125 (2018).

[26] K. S. Novoselov, A. K. Geim, S. V. Morozov, D. Jiang, Y. Zhang, S. V. Dubonos, I. V. Grigorieva, and A. A. Firsov, Electric field effect in atomically thin carbon films, Science **306**, 666 (2004).

[27] M. Shuichi, Phase transition between the quantum spin Hall and insulator phases in 3D: Emergence of a topological gapless phase, New J. Phys. **9**, 356 (2007).

[28] Y. Xu, F. Zhang, and C. Zhang, Structured Weyl Points in Spin-Orbit Coupled Fermionic Superfluids, Phys. Rev. Lett. **115**, 265304 (2015).

[29] M. Xiao, Q. Lin, and S. Fan, Hyperbolic Weyl Point in Reciprocal Chiral Metamaterials, Phys. Rev. Lett. **117**, 057401 (2016).

[30] C. Zhang, X.-Y. Ding, L.-Y. Gan, Y. Cao, B.-S. Li, X. Wu, and R. Wang, Symmetry-guaranteed ideal Weyl semimetallic phase in face-centered orthogonal C6, Phys. Rev. B **101**, 235119 (2020).

[31] A. A. Zyuzin, S. Wu, and A. A. Burkov, Weyl semimetal with broken time reversal and inversion symmetries, Phys. Rev. B **85**, 165110 (2012).

[32] D. F. Liu, A. J. Liang, E. K. Liu, Q. N. Xu, Y. W. Li, C. Chen, D. Pei, W. J. Shi, S. K. Mo, P. Dudin, T. Kim, C. Cacho, G. Li, Y. Sun, L. X. Yang, K. Z. Liu, S. S. P. Parkin, C. Felser, and Y. L. Chen, Magnetic Weyl semimetal phase in a Kagomé crystal, Science **365**, 1282 (2019).

[33] L. X. Yang, Z. K. Liu, Y. Sun, H. Peng, H. F. Yang, T. Zhang, B. Zhou, Y. Zhang, Y. F. Guo, M. Rahn, D. Prabhakaran, Z. Hussain, S. K. Mo, C. Felser, B. Yan, and Y. L. Chen, Weyl semimetal phase in the non-centrosymmetric compound TaAs, Nat. Phys. **11**, 728 (2015).

[34] H. M. Weng, C. Fang, Z. Fang, B. A. Bernevig, and X. Dai, Weyl Semimetal Phase in Noncentrosymmetric Transition-Metal Monophosphides, Phys. Rev. X **5**, 011029 (2015).

[35] I. Belopolski, P. Yu, D. S. Sanchez, Y. Ishida, T. R. Chang, S. S. Zhang, S. Y. Xu, H. Zheng, G. Chang, G. Bian, H. T. Jeng, T. Kondo, H. Lin, Z. Liu, S. Shin, and M. Z. Hasan, Signatures of a time-reversal symmetric Weyl semimetal with only four Weyl points, Nat. Commun. **8**, 942 (2017).

[36] B. Q. Lv, H. M. Weng, B. B. Fu, X. P. Wang, H. Miao, J. Ma, P. Richard, X. C. Huang, L. X. Zhao, G. F. Chen, Z. Fang, X. Dai, T. Qian, and H. Ding, Experimental Discovery of Weyl Semimetal TaAs, Phys. Rev. X **5**, 031013 (2015).

[37] L. Meng, Y. Li, J. Wu, L. Zhao, and J. Zhong, A type of novel Weyl semimetal candidate: Layered transition metal monochalcogenides $Mo_2XY$ ($X$, $Y$ = S, Se, Te, $X$ not equal $Y$), Nanoscale **12**, 4602 (2020).

[38] L. Meng, J. Wu, Y. Li, and J. Zhong, Dirac–Weyl semimetal phase in noncentrosymmetric transition metal monochalcogenides MoTe and WTe, J. Mater. Chem. C **7**, 12151 (2019).

[39] G. Kresse and J. Furthmüller, Efficiency of *ab-initio* total energy calculations for metals and semiconductors using a plane-wave basis set, Comput. Mater. Sci. **6**, 15 (1996).

[40] G. Kresse and D. Joubert, From ultrasoft pseudopotentials to the projector augmented-wave method, Phys. Rev. B **59**, 1758 (1999).

[41] J. P. Perdew, K. Burke, and M. Ernzerhof, Generalized Gradient Approximation Made Simple, Phys. Rev. Lett. **77**, 3865 (1996).

[42] A. Togo, F. Oba, and I. Tanaka, First-principles calculations of the ferroelastic transition between rutile-type and $CaCl_2$-type $SiO_2$ at high pressures, Phys. Rev. B **78**, 134106 (2008).

[43] Q. Wu, S. Zhang, H.-F. Song, M. Troyer, and A. A. Soluyanov, WannierTools: an open-source software package for novel topological materials, Comput. Phys. Commun. **224**, 405 (2018).

[44] X. L. Sheng, Q. B. Yan, F. Ye, Q. R. Zheng, and G. Su, T-Carbon: A Novel Carbon Allotrope, Phys. Rev. Lett. **106**, 155703 (2011).

[45] Y. Chen, Y. Y. Sun, H. Wang, D. West, Y. Xie, J. Zhong, V. Meunier, M. L. Cohen, and S. B. Zhang, Carbon Kagome Lattice and Orbital-Frustration-Induced Metal-Insulator Transition for Optoelectronics, Phys. Rev. Lett. **113**, 085501 (2014).

[46] N. P. Armitage, E. J. Mele, and A. Vishwanath, Weyl and Dirac semimetals in three-dimensional solids, Rev. Mod. Phys. **90**, 015001 (2018).

[47] D. Gresch, G. Autès, O. V. Yazyev, M. Troyer, D. Vanderbilt, B. A. Bernevig, and A. A. Soluyanov, Z2Pack: Numerical implementation of hybrid Wannier centers for identifying topological materials, Phys. Rev. B **95**, 075146 (2017).

[48] X. Wan, A. M. Turner, A. Vishwanath, and S. Y. Savrasov, Topological semimetal and Fermi-arc surface states in the electronic structure of pyrochlore iridates, Phys. Rev. B **83**, 205101 (2011).

[49] S.-Y. Xu, C. Liu, S. K. Kushwaha, R. Sankar, J. W. Krizan, I. Belopolski, M. Neupane, G. Bian, N. Alidoust, T.-R. Chang, H.-T. Jeng, C.-Y. Huang, W.-F. Tsai, H. Lin, P. P. Shibayev, F.-C. Chou, R. J. Cava, and M. Z. Hasan, Observation of Fermi arc surface states in a topological metal, Science **347**, 294 (2015).

[50] E. V. Gorbar, V. A. Miransky, I. A. Shovkovy, and P. O. Sukhachov, Origin of dissipative Fermi arc transport in Weyl semimetals, Phys. Rev. B **93**, 235127 (2016).

[51] S. Souma, Z. Wang, H. Kotaka, T. Sato, K. Nakayama, Y. Tanaka, H. Kimizuka, T. Takahashi, K. Yamauchi, T. Oguchi, K. Segawa, and Y. Ando, Direct observation of nonequivalent Fermi-arc states of opposite surfaces in the noncentrosymmetric Weyl semimetal NbP, Phys. Rev. B **93**, 161112(R) (2016).

[52] H. F. Yang, L. X. Yang, Z. K. Liu, Y. Sun, C. Chen, H. Peng, M. Schmidt, D. Prabhakaran, B. A. Bernevig, C. Felser, B. H. Yan, and Y. L. Chen, Topological Lifshitz transitions and Fermi arc manipulation in Weyl semimetal NbAs, Nat. Commun. **10**, 3478 (2019).

[53] G. Resta, S.-T. Pi, X. Wan, and S. Y. Savrasov, High surface conductivity of Fermi-arc electrons in Weyl semimetals, Phys. Rev. B **97**, 085142 (2018).

[54] See Supplemental Material at http://link.aps.org/supplemental/10.1103/PhysRevMaterials.5.104201 for the details of band structure of DHCN and the characteristics of some other crossing points in WSCN and DHCN.

[55] F. Ke, L. Zhang, Y. Chen, K. Yin, C. Wang, Y. -K. Tzeng, Y. Lin, H. Dong, Z. Liu, J. S. Tse, W. L. Mao, J. Wu, and B. Chen, Synthesis of atomically thin hexagonal diamond with compression, Nano. Lett. **20**, 5916 (2020).

[56] M. A. Hudspeth, B. W. Whitman, V. Barone, and J. E. Peralta, Electronic properties of the biphenylene sheet and its one-dimensional derivatives, ACS Nano **4**, 4565 (2010).